# A Novel Rotated Antenna Array Topology for Near-Field 3-D Fully Polarimetric Imaging

Wang, Jianping; Aubry, Pascal; Yarovoy, Alexander

**DOI**
10.1109/TAP.2018.2794408

**Publication date**
2018

**Document Version**
Final published version

**Published in**
IEEE Transactions on Antennas and Propagation

# Communication

## A Novel Rotated Antenna Array Topology for Near-Field 3-D Fully Polarimetric Imaging

Jianping Wang, Pascal Aubry, and Alexander Yarovoy

***Abstract*— In this communication, a novel approach to rotated antenna array topology design is proposed for fully polarimetric short-range imaging. The rotated antenna array proposed acquires two co-pol and one cross-pol signals in terms of the "local" polarization basis by means of three antenna pairs. Then, the fully polarimetric signals in a global polarization basis are retrieved via simple polarization basis transformation, which overcomes the spatially varied polarizations of the signals acquired at different positions and makes valid the assumption of traditional imaging algorithms that the polarization is constant within the aperture. The proposed rotated antenna array takes advantage of the synthetic aperture technique to synthesize a 2-D array for 3-D full-pol imaging. It utilizes a significantly smaller number of antennas in comparison to traditional fully polarimetric imaging arrays and also provides sufficiently accurate estimation to the full-pol electromagnetic signals scattered from targets. Both numerical simulations and experimental measurements have been performed and the results show the tolerance of the antenna array topology proposed to the quasi-monostatic measurements, its effectiveness, and accuracy for full-pol short-range microwave imaging.**

***Index Terms*— Fully polarimetric imaging, microwave imaging, rotated array, signal retrieval/estimation, ultrawideband (UWB) radar.**

### I. Introduction

Array-based microwave imaging has been widely used for remote sensing, security checks, and medical imaging [1]–[3]. The expansion of microwave imaging to various fields, especially short-range applications, and the demand for increasingly higher resolution and more accurate image reconstruction drive researchers to exploit the full advantages of wideband/ultrawideband (UWB) signals, antenna arrays, and polarimetry techniques and result in the development of sophisticated radar systems [4]–[6]. Taking advantage of wideband/UWB signals, high down-range resolution is achieved, while a large antenna array is required to achieve high cross-range resolution. Moreover, polarimetry technique exploits the vectorial nature of EM waves to explore subtle scattering features for target identification and recognition. As a consequence, polarimetric antenna arrays are essential for polarized EM signals acquisition.

Synthetic aperture radar technique, as a very important array technique, sequentially moves a single antenna/small array in space to synthesize an equivalently large aperture. It enables to significantly reduce the number of antennas needed in an antenna array system, thus saving the system cost as well as the space for its installation. So synthetic aperture technique provides a cost-efficient and compact array solution to imaging systems, which is extremely attractive for some excessively cost/space-limited circumstances, e.g., ground prediction system used for tunnel boring machine [7], [8].

According to imaging theory, a 2-D synthetic aperture is needed for 3-D imaging. In the open literature, several scanning approaches have been reported to synthesize a 2-D planar antenna array. The basic one is to move an antenna over a 2-D rectilinear grid. Using four different polarization combinations of transmitting-receiving antennas, fully polarimetric [i.e., horizontal–horizontal (HH), horizontal–vertical (HV), vertical–horizontal, and vertical–vertical (VV)] signals are acquired [6]. As the four polarimetric signals are typically measured at aligned polarization bases at all positions, each polarimetric component can be treated as scalar wave and some existing scalar-wave imaging algorithms are applicable for image formation [9], [10]. Then, four separate polarimetric images are obtained for the same scene to reveal different features of targets. Moreover, the four polarimetric components can also be arranged in a matrix and then processed by the matrix-based inversion method for image formation [11], [12]. Thus, all four polarimetric components are simultaneously integrated in one image.

Another scanning mechanism to synthesize a 2-D planar array is the rotated antenna array [13], [14] in which a linear array is generally used and rotated around a point. This approach is easy to implement, especially for 3-D short-range applications. However, for linearly polarized antenna array, this rotation constantly changes the polarization of the transmitting and receiving antennas within the synthetic aperture. It makes the traditional scalar-wave-based imaging algorithms and the matrix-based inversion approach not straightforwardly applicable. To address this problem, a rotated antenna array by measuring three co-pol data at each position was suggested for fully polarimetric imaging in [15]. Through a simple algebraic manipulation, the full-pol signals in an aligned polarization basis can be accurately estimated from the three co-pol measurements.

In this communication, a new approach to design rotated antenna array topology is proposed, as a companion to [15], for near-field 3-D fully polarimetric imaging, which requires to measure two co- and one cross-pol signals at each position in terms of the "local" polarization basis. Similar to the approach in [15], the proposed approach overcomes the spatially varied polarizations of signals within the rotated array aperture. It provides a supplement approach to rotated antenna array design within the framework derived in [15].

This communication is organized as follows. In Section II, the proposed approach and a designed rotated antenna array topology are presented. Then, its effectiveness and accuracy for full-pol signal acquisition are investigated in Section III. Section IV demonstrates the imaging performance of the proposed antenna array via both numerical simulations and experimental measurements. Finally, some conclusions are drawn in Section V.

### II. Signal Relations and Array Topology

Here, a new approach to rotated antenna array topology design is proposed based on (16) in [15]: a rotated array can measure

Manuscript received March 7, 2017; revised October 26, 2017; accepted December 26, 2017. Date of publication January 17, 2018; date of current version March 1, 2018. This work was supported by the NeTTUN project funded by the European Commission within the FP-7 Framework under Grant 280712. *(Corresponding author: Jianping Wang.)*

The authors are with the Faculty of Electrical Engineering, Mathematics and Computer Science, Delft University of Technology, 2628CD Delft, The Netherlands (e-mail: j.wang-4@tudelft.nl; p.j.aubry@tudelft.nl; a.yarovoy@tudelft.nl).

Color versions of one or more of the figures in this communication are available online at http://ieeexplore.ieee.org.

Digital Object Identifier 10.1109/TAP.2018.2794408

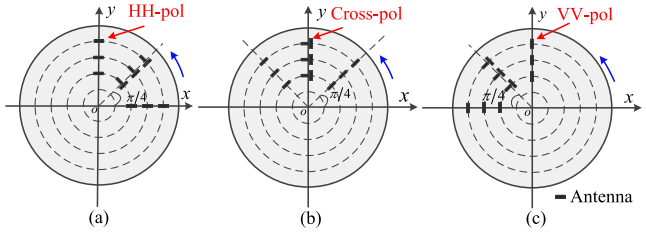


Fig. 1. Operating scheme of a rotated antenna array for full-polarimetric imaging. (a)–(c) Three instantaneous positions of the rotated antenna array during the operation.

two co- and one cross-pol signals in a "local" polarization basis at each position with its rotation for fully polarimetric imaging. As an example, a rotated antenna array topology designed with the proposed approach is shown in Fig. 1(a). The antennas are placed along three radii with different orientations (i.e., polarizations) over several concentric circles. One-third of the transceiver pairs of antennas is set with orientations normal to the radius and one-third with orientations parallel to the local radius. For another one-third of transceiver pairs, transmitting (receiving) antennas are arranged parallel to the radius, while receiving (transmitting) antennas are perpendicular to the radius.

With the rotation of the antenna array, it forms a 2-D circular antenna aperture. The rotated antenna array acquires two co-pol and one cross-pol signals with respect to the "local" polarization basis at each spatial position. Its operating scheme is illustrated in Fig. 1, which indicates three instantaneous array orientations at a sampling position on the $y$-axis. Utilizing the polarized components acquired at each position and the relations (16) in [15], the full polarimetric signals are retrieved in an aligned global polarization basis (i.e., H/V basis) for the full-pol imaging. For convenience, the relations (16) in [15] are rewritten as

$$\begin{cases} E^s_{\theta\theta}(\mathbf{x}^R, \mathbf{x}^T, \omega) = E_{11}\cos^2\theta - E_{12}\sin\ 2\theta + E_{22}\sin^2\theta \\ E^s_{\theta_\perp\theta}(\mathbf{x}^R, \mathbf{x}^T, \omega) = \dfrac{(E_{11}-E_{22})}{2}\sin\ 2\theta + E_{12}\cos 2\theta \\ E^s_{\theta\theta_\perp}(\mathbf{x}^R, \mathbf{x}^T, \omega) = \dfrac{(E_{11}-E_{22})}{2}\sin\ 2\theta + E_{12}\cos 2\theta \\ E^s_{\theta_\perp\theta_\perp}(\mathbf{x}^R, \mathbf{x}^T, \omega) = E_{11}\sin^2\theta + E_{12}\sin 2\theta + E_{22}\cos^2\theta \end{cases} \tag{1}$$

where $\mathbf{x}^R$ and $\mathbf{x}^T$ denote the positions of transmit and receive antennas, and $\theta$ is the angle from the positive horizontal axis to the antenna axis. For simplicity, $\theta$ and its normal direction $\theta_\perp$ are used as subscripts to indicate the corresponding polarization bases. So, the $E^s$s are the electric fields recorded in terms of the local polarization bases $(\theta, \theta_\perp)$, and $E_{11}, E_{12}, E_{22}$ are the electric fields obtained in the $H/V$ polarization bases. In both cases, the subscripts represent the receiving and transmitting antenna polarizations in order. Note that, in (1), the monostatic configuration is considered for the transmit and receive antennas, i.e., $\mathbf{x}^R = \mathbf{x}^T$.

## III. Performance Analysis of the Rotated Antenna Array for Full-Pol Signal Acquisition

The capability of the proposed rotated antenna array for full-pol signal acquisition was investigated by examining the accuracy of the retrieved full-pol signals with respect to the measurements taken by the traditional full-pol arrays (where the full-pol signals are generally measured in the aligned $H/V$ polarization bases). Meanwhile, its performance for full-pol signal estimation was also compared with that obtained with the rotated array proposed in [15]. For convenience

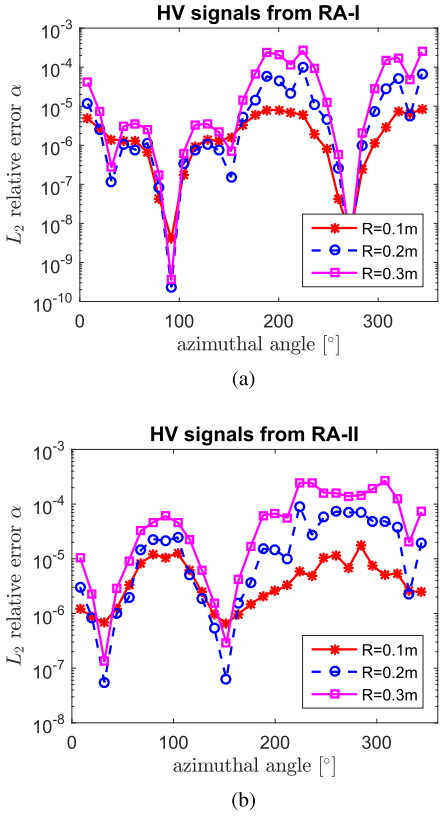


Fig. 2. $L_2$ relative errors of the retrieved cross-pol signals at some sampling positions over three circles of radii 0.1, 0.2, and 0.3 m within the aperture. (a) and (b) Relative errors of HV signals obtained with rotated arrays I and II, respectively.

of notation, array I refers to the rotated array topology proposed in this communication and array II for the rotated array in [15] and array III for the traditional full-pol antenna arrays in the following text.

In principle, the proposed approach to design rotated array topology is within the same framework in [15] derived based on the Born approximation. So, it is valid for point-like and weak scatterers. To examine the accuracy of the full-pol imaging for objects beyond the Born approximation with the proposed antenna array, numerical simulation was performed with a trihedral corner reflector (TCR). The TCR contains three mutually orthogonal surfaces with the shape as shown in Fig. 4(d), but their intersecting sides are 15 cm in length.

The simulation setup is similar to the experimental setup Fig. 4(a). For rotated antenna arrays (i.e., arrays I and II), the elementary dipole antennas were arranged along three radii according to their corresponding topologies. On each radius, 25 pairs of transceivers were placed from the radius of 2–50 cm with the interelement spacing of 2 cm. The rotated antenna arrays take samples every 4° in azimuth during the rotation. As a result, a circular antenna aperture of radius 0.5 m was synthesized. Taking the same spatial samples, the traditional full-pol antenna arrays (array III) were also constructed with the transceivers in an aligned polarization basis within the aperture. All the antenna arrays were placed on the $x$–$z$ plane and centered at the origin. The $y$-axis points toward the TCR, which is placed 0.4 m away from the antenna aperture. Then, the synthetic data were generated by EM software FEKO in the frequency domain with operational frequencies sweeping from 2 to 12 GHz with steps of 100 MHz.

After obtaining the frequency-domain synthetic data, they were transformed to time domain using fast Fourier transform (FFT) with a Hanning window. Taking advantage of the signals acquired with

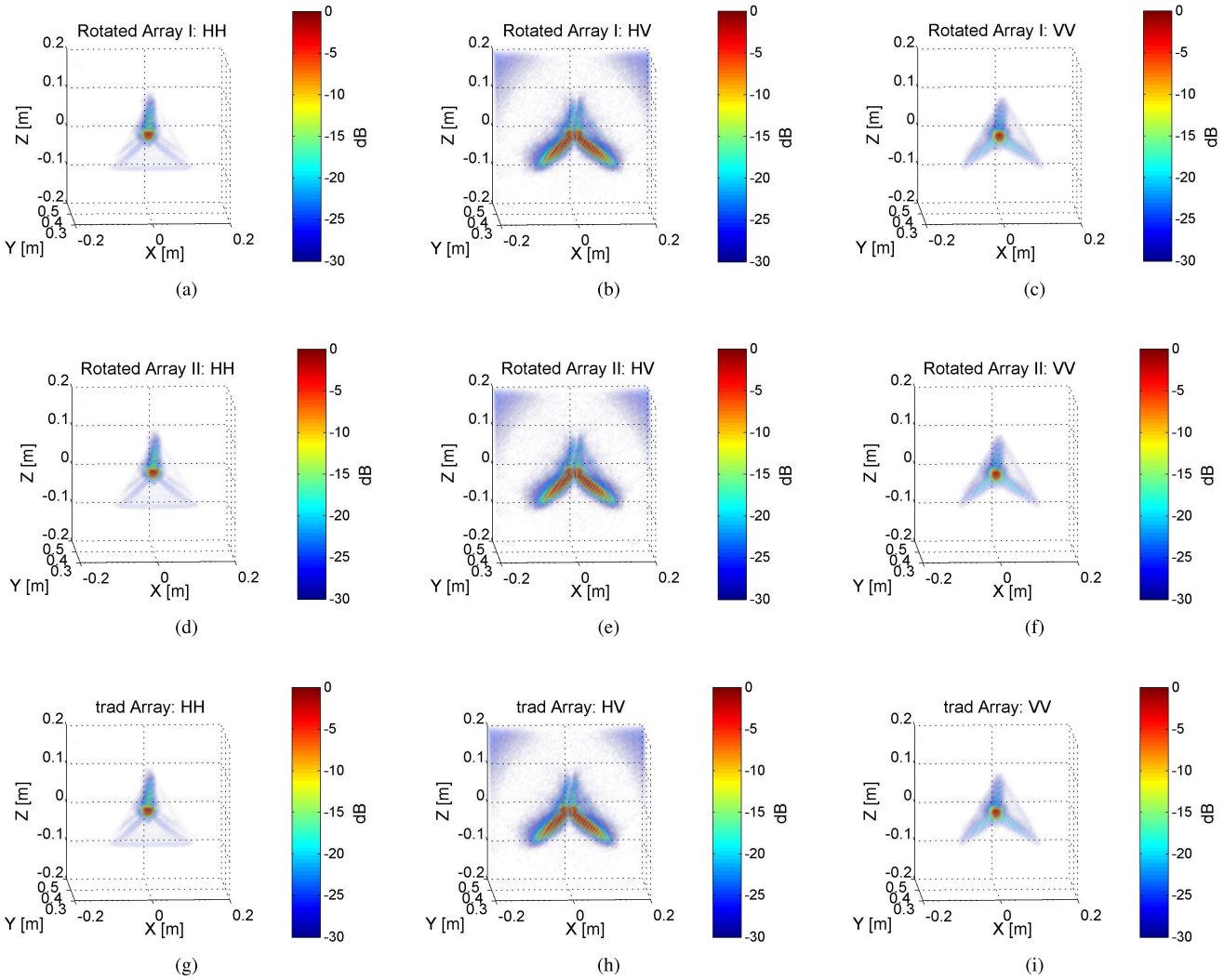


Fig. 3. HH-, HV-, and VV-pol images reconstructed with the three different antenna arrays. (a)–(c) Images obtained with the rotated antenna array by acquiring two co-pol and one cross-pol signals at each position (array I). (d)–(f) Images obtained with the rotated antenna array by acquiring three co-pol signals at each position (array II). (g)–(i) Images obtained with traditional antenna arrays (array III).

arrays I and II, the corresponding full-pol signals were estimated via (1) and (17) in [15], respectively. To evaluate the accuracy of the estimated full-pol signals, the $L_2$ relative error defined by (20) in [15] is used as a metric. Generally, the $L_2$ relative errors of the retrieved co-pol signals are very small, i.e., much less than $5 \times 10^{-3}$. Among differently polarized signals, the largest relative errors are observed for the retrieved cross-pol signals. Fig. 2 shows the $L_2$ relative errors of the retrieved cross-pol signals at some sampling positions over three circles of the radius 0.1, 0.2, and 0.3 m within the aperture. From Fig. 2(a), one can see that the relative errors of HV signals retrieved with rotated Array I are generally smaller than $2 \times 10^{-3}$. Compared with Fig. 2(b), rotated array I obtains comparable accuracy for the retrieved HV signals as the rotated array II. In addition, due to the direct acquisition of cross-pol signals in a local polarization basis, the rotated array I results in much smaller relative errors, down to about $10^{-10}$ compared with the rotated array II.

## IV. Imaging Experiments

In this section, numerical simulations and experimental measurements are presented to demonstrate the fully polarimetric imaging performance of the rotated antenna arrays.

### A. Numerical Results

First, the synthetic data of the TCR used for signal analysis were used for full-pol imaging. Focusing the polarimetric signals estimated with the two rotated antenna arrays (i.e., arrays I and II), the HH-, HV-, and VV-polarimetric images of the TCR were reconstructed, which are shown in Fig. 3(a)–(f). Meanwhile, the fully polarimetric images acquired with the traditional full-pol antenna arrays are also presented as references, as shown in Fig. 3(g)–(i).

From Fig. 3, one can see that all the images obtained with the three antenna arrays are well focused and different scattering features of the TCR are exposed in the HH-, HV-, and VV-polarimetric images. For instance, the edge of the bottom surface is well reconstructed in the HH-pol images, while the edges of the two top surfaces are clearly presented in the VV-pol images. Meanwhile, the HH- and VV-pol images distinctly show the three intersecting sides of the surfaces and the corner point appears as the brightest spot.In the HV-pol images, the two bottom intersecting sides demonstrate the strongest cross-polarization effects with the orientation of the TCR placed in the simulation. As its projection on the antenna aperture is a vertical line, the top intersecting side induces negligible cross-polarized signals. Thus, it is missing in the focused HV-polarized images [i.e., the middle

TABLE I

ACCURACY OF THE POLARIMETRIC IMAGES OF THE TCR OBTAINED WITH THE ROTATED ARRAYS AND THE TRADITIONAL ARRAYS

| | | HH | HV | VV |
|---|---|---|---|---|
| Roated Array I | $L_2$ error | 1.6374e-6 | 2.6249e-5 | 1.6333e-6 |
| | $L_\infty$ error | 5.5975e-4 | 3.89e-3 | 5.4874e-4 |
| Rotated Array II | $L_2$ error | 2.1335e-13 | 1.733e-5 | 2.1401e-13 |
| | $L_\infty$ error | 3.0898e-8 | 3.578e-3 | 3.2136e-8 |

slits in Fig. 3(b), (e), and (h)]. Comparing the polarimetric images in each column, the HH-, HV-, and VV-pol images obtained with the two rotated antenna arrays and the traditional arrays are visually equivalent.

To quantitatively investigate the accuracy of the images obtained with arrays I and II, the $L_2$ and $L_\infty$ errors were used to examine their differences from the reference counterparts. The $L_2$ relative error is defined as (20) in [15] by replacing the signal samples with the voxel values of the polarimetric images. The $L_\infty$ error is defined as the maximum voxel value difference divided by the maximum voxel value of the reference image. The relative errors of the reconstructed images with respect to the reference images are listed in Table I. One can see that array I achieves roughly uniform $L_2$ and $L_\infty$ errors for different polarimetric images, while the relative errors of HH- and VV-pol images obtained with array II are much smaller than that of the HV-pol image. But the accuracies of the HV-pol images acquired with arrays I and II are comparable (i.e., about $10^{-5}$ for $L_2$ error and $10^{-3}$ for $L_\infty$ error). Therefore, sufficient accuracies, even for strong scattering objects, are achieved by both Arrays I and II for full-pol imaging although some subtle differences are observed in the accuracies of their full-pol images.

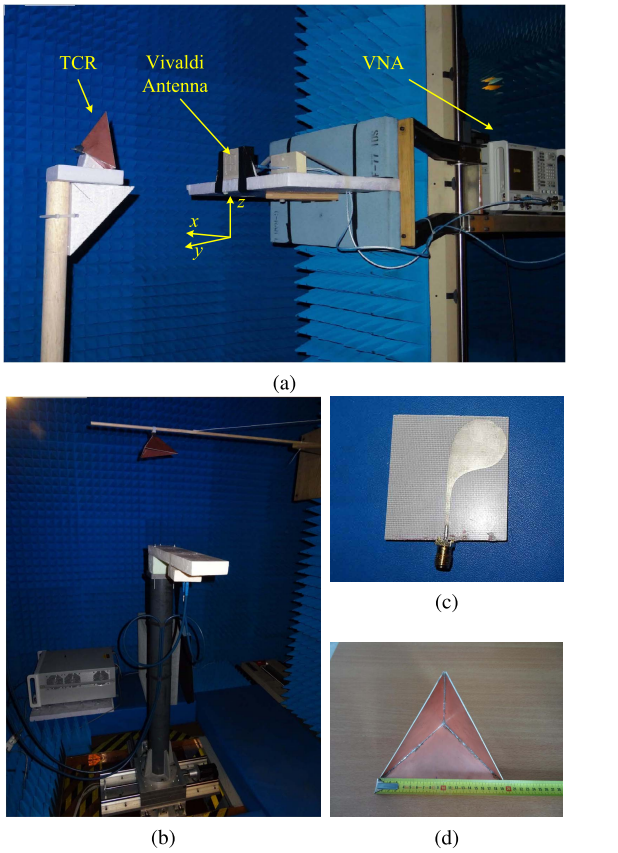


Fig. 4. Experimental setups for rotated arrays and traditional full-pol antenna arrays. (a) Setup for traditional polarimetric arrays. (b) Measurement setup for rotated antenna arrays. (c) Antipodal Vivaldi antenna used for measurement. (d) TCR.

### *B. Experimental Measurements*

For experimental measurements, the two rotated antenna arrays (i.e., arrays I and II) and the traditional arrays (array III) were implemented with two different setups. The measurement setup for the rotated arrays is shown in Fig. 4(b). A column has been installed on a pedestal that can be linearly translated and rotated by a step motor that has been precisely controlled by a computer. And a polyethylene panel was put on the top of the column as a support for transceivers. Here, the antipodal Vivaldi antennas were used for transmitting and receiving and connected to a vector network analyzer (VNA). To overcome the effects of quasi-monostatic configuration on the signal estimation mentioned in [15], here $S_{11}$ was measured to get the co-pol components for monostatic radar, and only the cross-pol components were recorded with a quasi-monostatic configuration by measuring $S_{21}$, where a transmitting antenna and a receiving antenna were placed with a separation of 6 cm. Similar to the simulation, a TCR was used as an object and its edge lengths are about 19.7 cm, as shown in Fig. 4(d). The TCR was placed in front of the antenna aperture at a distance of 0.5 m. The operational frequencies were from 3 to 15 GHz with steps of 20 MHz. By driving the step motor, the antennas were rotated in azimuth and translated in the radial direction to acquire signals over 15 concentric circles with radii ranging from 11 to 53 cm with steps of 3 cm and the azimuthal sampling interval on the circles was 1.2°. So, a circular aperture of radius 0.53 m was synthesized.

The traditional antenna arrays were implemented by a planar scanner. The fully polarimetric, i.e., HH-, HV-, and VV-pol signals, were recorded over the same sampling grids as the rotated antenna arrays and the experimental setup is shown in Fig. 4(a). To suppress the effects of the background scattering and antenna coupling, measurements were conducted both with and without the presence of the object for all three antenna arrays. The frequency-domain signals measured with the VNA were converted to the time domain via the FFTafter applying a Hanning window.

Taking background subtraction and image focusing, the fully polarimetric images were obtained. The focused images obtained with the two rotated arrays and the traditional arrays are shown in Fig. 5. It can be seen that both rotated antenna arrays reconstruct the comparable polarimetric features of the TCR in the corresponding images in contrast to the traditional arrays. However, some differences are still noticeable between the polarimetric images formed with the two rotated arrays. Visually, the rotated antenna array I achieves slightly better fully polarimetric images in terms of the similarity to those obtained with the traditional arrays. More specifically, in both HH- and VV-pol images obtained with rotated antenna array II the edges along the $z$-axis direction are much weaker than that in the corresponding images of rotated antenna array I. Moreover, the cross-pol image focused with rotated array II [Fig. 5(e)] is slightly asymmetric with respect to the $xoy$ plane compared to that obtained with rotated array I [Fig. 5(b)]. Also, the sidelobes/artifacts surrounding the images of the TCR seem slightly rotated. These may be caused by nonpurity of the linear polarization of the antipodal Vivaldi antenna used for the measurement, especially for high frequencies. As a consequence, cross-pol signals were inaccurately estimated with the measurements of the rotated antenna array II. However, in the rotated antenna array I, the cross-pol signals in a "local" polarization basis were measured with two orthogonally oriented Vivaldi antennas at

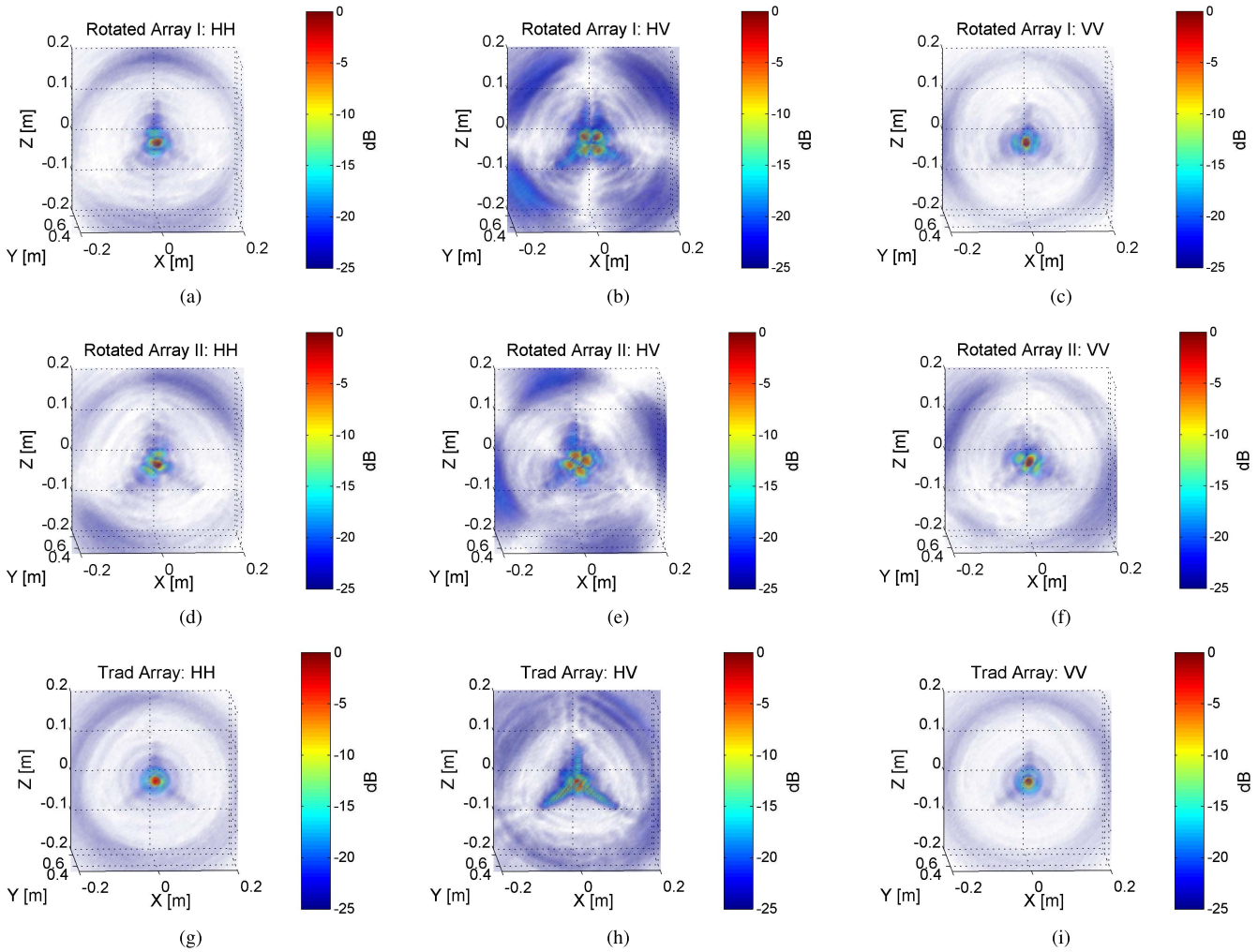


Fig. 5. 3-D polarimetric images of a TCR formed with the experimental measurements by the three antenna arrays. (a)–(c) HH-, HV-, and VV-pol images focused with the measurements of rotated antenna array I. (d)–(f) Measurements of rotated antenna array II. (g)–(i) Measurements of traditional antenna arrays (array III).

each spatial position, which to some extent mitigates the effect of the nonpurity of their linear polarization on the HV-pol signal estimation.

Furthermore, only the HV-pol image, which is obtained with the rotated Array I [Fig. 5(b)], reveals the slit induced by the intersecting side formed by the two top surfaces in a full agreement with the HV-pol images in Fig. 3 obtained in the numerical simulations, while two other HV-pol images [Fig. 5(e) and (h)] obtained in the quasi-monostatic configuration fail to show this slit. This demonstrates further the effectiveness and accuracy of the proposed rotated array for fully polarimetric imaging and indicates relatively higher tolerance of the array I to the quasi-monostatic measurement configuration for accurate full-pol imaging compared to the array II and the traditional fully polarimetric arrays. This advantage could be very attractive for the implementation of practical full-pol imaging systems, especially in the circumstances, where antennas with relatively lower cross-pol isolation are used.

## V. Conclusion

A new approach to rotated antenna array topology design for near-field 3-D fully polarimetric imaging has been proposed. With the proposed approach, the designed antenna array acquires two co- and one cross-pol signals at each spatial sampling position using three different antenna pairs. By a simple linear algebraic manipulation, the full-pol signals in an aligned polarization coordinate system can be accurately estimated, which facilitates the traditional scalar-wave-based imaging algorithms for full-pol imaging. Based on the proposed approach, an example of the rotated antenna array topology was presented. Despite being based on the Born approximation, according to both numerical simulations and experiments, the rotated antenna array topology proposed enables to reconstruct accurate (similar to the traditional full-pol arrays) fully polarimetric target responses and images, even for strong scattering objects. Furthermore, the experimental measurements reveal that the designed rotated array topology is less sensitive to the nonpurity of the linear polarization of antennas and also have higher tolerance to quasi-monostatic configuration in the cross-pol measurement for accurate full-pol imaging compared to the state of the art. These features will benefit the implementation of the practical full-pol imaging systems, especially where antennas have relatively low cross-pol isolations.

## References

[1] J.-S. Lee and E. Pottier, *Polarimetric Radar Imaging: From Basics to Applications*. Boca Raton, FL, USA: CRC Press, 2009.

[2] D. M. Sheen, D. L. McMakin, and T. E. Hall, "Three-dimensional millimeter-wave imaging for concealed weapon detection," *IEEE Trans. Microw. Theory Techn.*, vol. 49, no. 9, pp. 1581–1592, Sep. 2001.

[3] X. Li, E. J. Bond, B. D. V. Veen, and S. C. Hagness, "An overview of ultra-wideband microwave imaging via space-time beamforming for early-stage breast-cancer detection," *IEEE Antennas Propag. Mag.*, vol. 47, no. 1, pp. 19–34, Feb. 2005.

[4] J. D. Taylor, *Introduction to Ultra-Wideband Radar Systems*. New York, NY, USA: Taylor & Francis, 1994. [Online]. Available: https://books.google.nl/books?id=vkTSTfvgDZoC

[5] J. L. Schwartz and B. D. Steinberg, "Ultrasparse, ultrawideband arrays," *IEEE Trans. Ultrason., Ferroelect., Freq. Control*, vol. 45, no. 2, pp. 376–393, Mar. 1998.

[6] R. Salman, I. Willms, L. Reichardt, T. Zwick, and W. Wiesbeck, "On polarization diversity gain in short range UWB-Radar object imaging," in *Proc. IEEE Int. Conf. Ultra-Wideband (ICUWB)*, Sep. 2012, pp. 402–406.

[7] T. Sato, K. Takeda, T. Nagamatsu, T. Wakayama, I. Kimura, and T. Shinbo, "Automatic signal processing of front monitor radar for tunneling machines," *IEEE Trans. Geosci. Remote Sens.*, vol. 35, no. 2, pp. 354–359, Mar. 1997.

[8] J. Wang, H. Cetinkaya, A. Yarovoy, I. I. Vermesan, and S. Reynaud, "Investigation of forward-looking synthetic circular array for subsurface imaging in tunnel boring machine application," in *Proc. 8th Int. Workshop Adv. Ground Penetrating Radar (IWAGPR)*, 2015, pp. 1–4.

[9] J. W. Wiggins, "Kirchhoff integral extrapolation and migration of nonplanar data," *Geophysics*, vol. 49, no. 8, pp. 1239–1248, 1984.

[10] J. M. Lopez-Sanchez and J. Fortuny-Guasch, "3-D radar imaging using range migration techniques," *IEEE Trans. Antennas Propag.*, vol. 48, no. 5, pp. 728–737, May 2000.

[11] J. van der Kruk, C. P. Wapenaar, J. T. Fokkema, and P. M. van den Berg, "Three-dimensional imaging of multicomponent ground-penetrating radar data," *Geophysics*, vol. 68, no. 4, pp. 1241–1254, 2003.

[12] R. Streich and J. van der Kruk, "Accurate imaging of multicomponent gpr data based on exact radiation patterns," *IEEE Trans. Geosci. Remote Sens.*, vol. 45, no. 1, pp. 93–103, 2007.

[13] Z. Li, J. Wang, J. Wu, and Q. H. Liu, "A fast radial scanned near-field 3-d sar imaging system and the reconstruction method," *IEEE Trans. Geosci. Remote Sens.*, vol. 53, no. 3, pp. 1355–1363, 2015.

[14] S. Zhu, W. Jian, L. Yu, S. Yi, and M. Sato, "A circular measurement for linearly polarized ground penetrating radar to map subsurface crossing cylinders," in *Proc. IEEE Int. Geosci. Remote Sens. Symp. (IGARSS)*, Jul. 2013, pp. 1426–1429.

[15] J. Wang, P. Aubry, and A. Yarovoy, "A novel approach to full-polarimetric short-range imaging with copolarized data," *IEEE Trans. Antennas Propag.*, vol. 64, no. 11, pp. 4733–4744, Nov. 2016.